Ion transport and selectivity in nanopores with spatially inhomogeneous fixed charge distributions

Patricio Ramírez[a)] and Vicente Gómez
Departament de Física Aplicada, Universitat Politècnica de València, Camino de Vera s/n,
E-46022 Valencia, Spain

Javier Cervera
Departament de Ciències Experimentals, Universitat Jaume I, Apartado 224, E-12080 Castelló, Spain

Birgitta Schiedt
Gesellschaft für Schwerionenforschung (GSI), Planckstrasse 1, D-64291 Darmstadt, Germany

Salvador Mafé
Departament de Termodinàmica, Universitat de València, E-46100 Burjassot, Spain

Polymeric nanopores with fixed charges show ionic selectivity when immersed in aqueous electrolyte solutions. The understanding of the electrical interaction between these charges and the mobile ions confined in the inside nanopore solution is the key issue in the design of potential applications. The authors have theoretically described the effects that spatially inhomogeneous fixed charge distributions exert on the ionic transport and selectivity properties of the nanopore. A comprehensive set of one-dimensional distributions including the skin, core, cluster, and asymmetric cases are analyzed on the basis of the Nernst-Planck equations. Current-voltage curves, nanopore potentials, and transport numbers are calculated for the above distributions and compared with those obtained for a homogeneously charged nanopore with the same average fixed charge concentration. The authors have discussed if an appropriate design of the spatial fixed charge inhomogeneity can lead to an enhancement of the transport and selectivity with respect to the homogeneous nanopore case. Finally, they have compared the theoretical predictions with relevant experimental data. © *2007 American Institute of Physics.* [DOI: 10.1063/1.2735608]

I. INTRODUCTION

Ion channels are natural nanopores with fixed charges that occur in most biological membranes.[1] Polymeric, fixed charge nanopores of dimensions comparable to the size of biological macromolecules such as proteins[2–4] and DNA (Refs. 5–7) have potential applications in single particle detection, analysis, and separation of biomolecules. When immersed in aqueous electrolyte solutions, the resulting membranes show ionic selectivity, favoring the passage of counterions (ions with charge opposite to that of the pore) but hindering the passage of coions (ions with charge of the same sign as the pore). A clear, fundamental understanding of the electrical interaction between the nanopore fixed charges and the mobile ions confined in the nanopore solution is needed for the design of practical applications.[5–11]

Since most nanopore fixed charge distributions deviate to some extent from homogeneity, the question of how inhomogeneous distributions affect the transport and selectivity of the nanopore naturally arises.[9–13] This problem has previously been discussed in the context of macroscopic ion-exchange membranes[14–22] as well as in some biological ion channels recently,[23–26] but it has not still received a systematic attention in the case of nanopores except for the case of conically shaped geometries with asymmetric fixed charge distributions, which have been analyzed by Karnik *et al.*,[8] Siwy and co-workers,[9,12] and Ramírez and co-workers.[10,11] However, studying a comprehensive survey of fixed charge distributions systematically is of great interest both because of the need of a better understanding of the processes occurring in supposedly homogeneous nanopores and the possibility of designing and exploiting the inhomogeneity effects in practical applications.[12,26–29] In particular, asymmetric fixed charge distributions are useful for rectifying junctions[26,30,31] and single molecule sensing.[32,33] Although the effects of asymmetry are conveniently explained in terms of the axial electric potential profile,[9,11,13,28] the nanopore charge distribution is the source of the electric field and dictates therefore the particular transport and selectivity properties in each case.

We have described theoretically the effects that typical fixed charge distributions exhibiting spatial variation over the macroscopic nanopore length exert on the transport and selectivity properties. To this end, we have disregarded the nanopore geometrical details assuming that they lead eventually to the different effective charge distributions considered here. This allows analyzing thoroughly a comprehensive set of one-dimensional distributions that include most cases of practical interest on the basis of the Nernst-Planck equations.[1,12,17,34,35] For each distribution, we have calculated the current-voltage (*I-V*) curve, the nanopore potential

a)Electronic mail: patraho@fis.upv.es
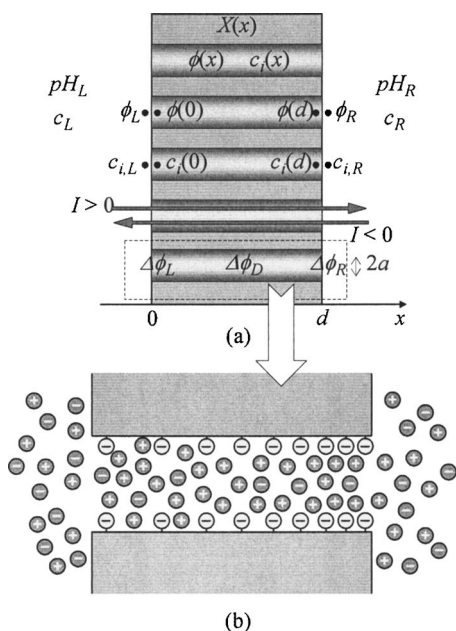
126, 194703-1

FIG. 1. Schematic view of the nanopore [Fig. 1(a)] and the inside solution with the mobile positive and negative ions as well as the negative fixed charge groups [Fig. 1(b)].

as a function of the external ion concentrations, and the counterion transport number (a measure of the nanopore selectivity[35]). The results have been compared with those obtained for the case of a homogeneously charged nanopore with the same average fixed charge concentration. In particular, we have discussed if the occurrence of spatial inhomogeneities in the fixed charge can lead to an enhancement of the transport and selectivity with respect to the homogeneous nanopore case[36] and contrasted the theoretical predictions with recent experimental data. Since nanopores with fixed charges display properties that resemble those found in protein ion channels such as ionic selectivity and current rectification,[1,24–28,33–35] reference to some asymmetric channels is also made.

II. THEORETICAL MODEL

Figure 1(a) shows schematically a polymeric film, containing cylindrical nanopores of thickness d and radius a, which separates two electrolyte solutions (KCl in our case). $X(x)$ is the total fixed charge concentration at a point of coordinate x within the pore [see Fig. 1(b), where an inhomogeneous fixed charge distribution $X(x)$ along the pore is represented]. $c_i(x)$ and $\phi(x)$ are, respectively, the local concentration of the species $i(i=K^+,Cl^-)$ and the electric potential in RT/F units, where R, T, and F have their usual meanings.[9] $c_{i,j}$ is the concentration of the species i in the bulk of the bathing solution j ($j=L$ for the left and $j=R$ for the right bathing solutions) and c_j, ϕ_j, and $pH_j(j=L,R)$ refer to the electrolyte concentration, the dimensionless electric potential and the pH value of the solution j, respectively. The potential drops $\Delta\phi_L=\phi(0)-\phi_L$ and $\Delta\phi_R=\phi_R-\phi(d)$ are, respectively, the Donnan potential differences through the left and right interfaces, and $\Delta\phi_D=\phi(d)-\phi(0)$ is the diffusion potential within the pore. We assume that the bathing solu-

tions are ideal and perfectly stirred, and that the whole system is isothermal. Although the present model has been developed for synthetic nanopores, it can be extended to the case of synthetic ion exchange membranes and biological ion channels of mesoscopic size.

Figure 2 illustrates six of the axial profiles $X(x)$ studied. We consider first only negative fixed charge groups (in the case of synthetic track-etched nanopores, the fixed charge groups are carboxylic moieties generated by a track-etching process[33,37,38]). The axial profiles correspond to typical symmetric and asymmetric pores and include most of the cases that could be found in practical situations. The skin and core distributions may result from usual membrane preparation procedures (see, e.g., Refs. 14–17 and 22 as well as references therein) and could also find application in the case of double conical track-etched pores. The cluster distributions are typical of pores where a hydrophobic structure is superimposed to clusterlike hydrophilic regions containing the charged groups, the water molecules, and the mobile ions (see, e.g., Ref. 14 and references therein). Finally, asymmetric distributions are common place and include conical track-etched nanopores,[12,13,33] ion channels,[24–26] and bipolar junctions.[30,31] Interestingly, symmetric or quasisymmetric synthetic pores and ion channels can also exhibit asymmetrical properties: a pH difference imposed in the external solutions can produce a variable concentration of the dissociated weak-acid fixed groups through the nanopore.[9,26]

It has recently been shown that the fixed charges in the nanopore are largely responsible for the transport and selectivity phenomena observed.[2–11] The electrostatic interaction between these and the mobile charges can approximately be described with relatively simple continuum models when the nanopore radius is larger than the screening Debye length and the typical ion size.[10,11,39,40] Some of the models considered previously are based on the Nernst-Planck and Poisson equations[10,11] that allow to obtain the profiles of electric potential and average concentration of mobile ions along the pore. However, they are rather cumbersome and we can employ also other approximated models[39,40] that clearly show the essential qualitative characteristics of the problem. We will use here one of these approaches which is based on the the Nernst-Planck flux equations together with the electroneutrality assumption. We expect this assumption to be approximately valid for the charge distributions of Fig. 2 that show spatial inhomogeneities extending over the macroscopic nanopore length (typically about $10–100$ μm for artificial nanopores[17]). We recall that the electroneutrality condition is essentially valid for one-dimensional ion transport problems where the axial coordinate extends over regions much thicker than the typical Debye length.[17,41]

The ionic transport through the cylindrical nanopore is described by the Nernst-Planck equations,

$$J_i=-D_i\frac{dc_i}{dx}-z_iD_ic_i\frac{d\phi}{dx}, \quad i=K^+,Cl^-, \qquad (1)$$
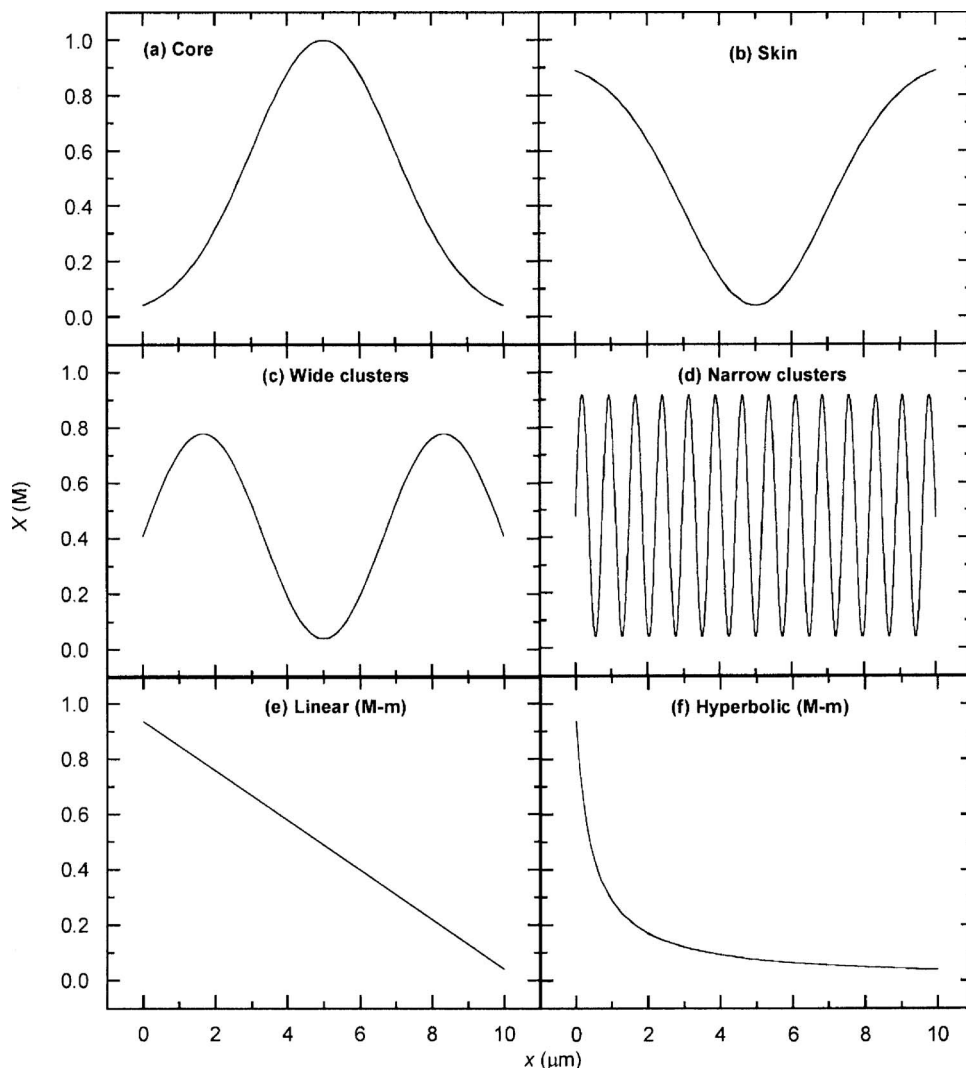
together with the steady state continuity equations,

FIG. 2. Axial profiles of the fixed charge concentration $X(x)$ through the nanopore.

$$\frac{dJ_i}{dx} = 0, \quad i = K^+, Cl^-, \tag{2}$$

and the electroneutrality equation,

$$\sum_i z_i c_i + \omega X = 0, \tag{3}$$

where ω is the sign of the fixed charges. In Eqs. (1)–(3) J_i, D_i, and z_i denote the ionic flux, the diffusion coefficient, and the charge number of species i, respectively. External and membrane solution concentrations are connected through the Donnan equilibrium conditions[35] at interfaces $x=0$ and $x=d$,

$$c_i(0) = c_{i,L} \exp(-z_i \Delta \phi_L) = c_L \exp(-z_i \Delta \phi_L),$$
$$i = K^+, Cl^-, \tag{4a}$$

$$c_i(d) = c_{i,R} \exp(z_i \Delta \phi_R) = c_R \exp(z_i \Delta \phi_R), \quad i = K^+, Cl^-, \tag{4b}$$

where the specific ionic partition coefficients between the external and the membrane solutions[35] are assumed to be unity. Combining Eqs. (3) and (4), the concentration of the ionic species at the pore/solution interfaces are

$$c_i(0) = -z_i \frac{\omega X(0)}{2} + \sqrt{\left[\frac{X(0)}{2}\right]^2 + c_L^2}, \quad i = K^+, Cl^-, \tag{5a}$$

$$c_i(d) = -z_i \frac{\omega X(d)}{2} + \sqrt{\left[\frac{X(d)}{2}\right]^2 + c_R^2}, \quad i = K^+, Cl^-. \tag{5b}$$

The discontinuous Donnan approach is approximately valid here because the nanopore thickness is much greater than the Debye length of the problem.[42,43] The I-V curve of the nanopore can be obtained as follows. For a total electric current,

$$I = \pi a^2 \sum_i z_i F J_i, \tag{6}$$

integration of Eqs. (1)–(3) with the boundary conditions of Eq. (5) provides the ionic fluxes J_i and the ionic concentration and electric potential profiles $c_i(x)$ and $\phi(x)$. From these profiles, the voltage $V = RT(\phi_L - \phi_R)/F$ applied to the nanopore is obtained. We refer to the potential difference obtained in the case $I=0$ as the *nanopore potential*, analogous to the *membrane potential* found in membrane science.[35]

We have solved Eqs. (1)–(3) using the shooting method.[44] As initial values, we have employed the ionic
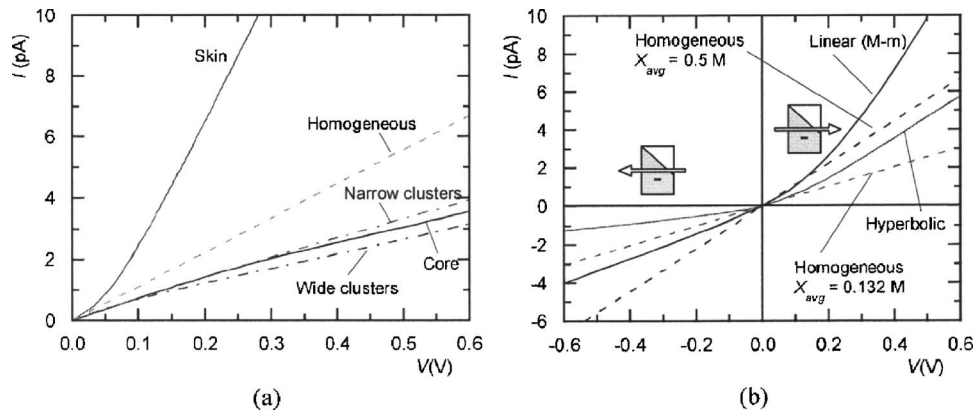
FIG. 3. *I-V* curves for the symmetrical [Fig. 3(a)] and asymmetrical [Fig. 3(b)] fixed charge distributions of Fig. 2 with $c_L=c_R=0.1M$. The arrows in the insets indicate the direction of the current with respect to X_M and X_m. Dashed lines correspond to homogeneous charge distributions with the same average concentrations (0.5M for the linear case, 0.132M for the hyperbolic case).

fluxes given by the Goldman constant field (GCF) approximation, which considers a constant electric field through the nanopore[45–47] and allows linearizing the Nernst-Planck equations. This assumption leads to simple analytic solutions for the fluxes of the different ionic species,

$$J_i \approx z_i \frac{D_i \Delta\phi_D}{d} \frac{c_i(0)\exp(-z_i\Delta\phi_D) - c_i(d)}{1 - \exp(-z_i\Delta\phi_D)}, \quad i = K^+, Cl^-,$$

(7)

where the diffusion potential $\Delta\phi_D = \phi(d) - \phi(0)$ is obtained from the total applied voltage,

$$V = RT(\phi_L - \phi_R)/F = -RT(\Delta\phi_L + \Delta\phi_D + \Delta\phi_R)/F,$$ (8)

for $I \neq 0$. In the case $I = 0$, this potential is[45,46]

$$\Delta\phi_D = \ln\frac{D_{K^+}c_{K^+}(0) + D_{Cl^-}c_{Cl^-}(d)}{D_{K^+}c_{K^+}(d) + D_{Cl^-}c_{Cl^-}(0)}.$$

(9)

The GCF assumption provides useful analytical solutions of the above transport equations for membranes and nanopores with homogeneous fixed charge distributions. Previous calculations (not discussed here) show that this assumption also gives fairly good results for inhomogeneous distributions when the charge profile varies smoothly.

The concentration distributions of Fig. 2 are assumed to correspond to negative fixed charges and can conveniently be written as

(i) Core distribution [Fig. 2(a)]

$$X(x) = X_M \exp\left[-\frac{(x-d/2)^2}{B^2}\right], \quad B^2 \equiv \frac{d^2}{4\ln(X_M/X_m)}.$$

(10)

(ii) Skin distribution [Fig. 2(b)]

$$X(x) = X_M + X_m - X_M \exp\left[-\frac{(x-d/2)^2}{B^2}\right],$$

(11)

$$B^2 \equiv \frac{d^2}{4\ln(X_M/X_m)}.$$

(iii) Cluster distribution [Figs. 2(c) and 2(d)]

$$X(x) = (X_M/2)\sin\left[\frac{2\pi x}{(2d/3^n)}\right] + (X_M/2) + X_m, \quad X_M \gg X_m,$$

(12)

where $n=1$ for wide clusters [Fig. 2(c)] and $n=3$ for narrow clusters [Fig. 2(c)].

(iv) Linear distribution [Fig. 2(e)]

$$X(x) = \frac{X_M - X_m}{d}x + X_M.$$

(13)

(v) Hyperbolic distribution [Fig. 2(f)]

$$X(x) = \frac{X_M}{1 - (1 - X_M/X_m)x/d}.$$

(14)

In all cases, X_M and X_m refer to the maximum and minimum values of the fixed charge concentration, respectively.

III. RESULTS AND DISCUSSION

The model calculations presented here are intended to emphasize the essential qualitative trends of the different fixed charge distributions rather than to analyze quantitatively the transport properties of a particular nanopore. However, the theoretical results are validated by comparison with recent experimental data relevant to each nanopore fixed charge distribution.

We have considered the nanopore thickness $d=10$ μm and radius $a=3$ nm as typical values.[9–11,33] Also, we have employed the (infinite dilution) diffusion coefficients of the ionic species $D_{K^+}=1.95\times10^{-5}$ cm^2/s and $D_{Cl^-}=2.03\times10^{-5}$ cm^2/s. For the fixed charge concentration, we have assumed $X_M=1M$ and $X_m=0.04M$ in the core distribution of Fig. 2(a). The extreme values X_M and X_m for the distributions in Figs. 2(b)–2(e) have then been chosen to give the same average concentration,

$$X_{avg} = \frac{1}{d}\int_0^d X(x)dx \approx 0.5M,$$

(15)

keeping constant the minimum value $X_m=0.04M$ in each case. Fixing X_{avg} and X_m allows a better comparison between
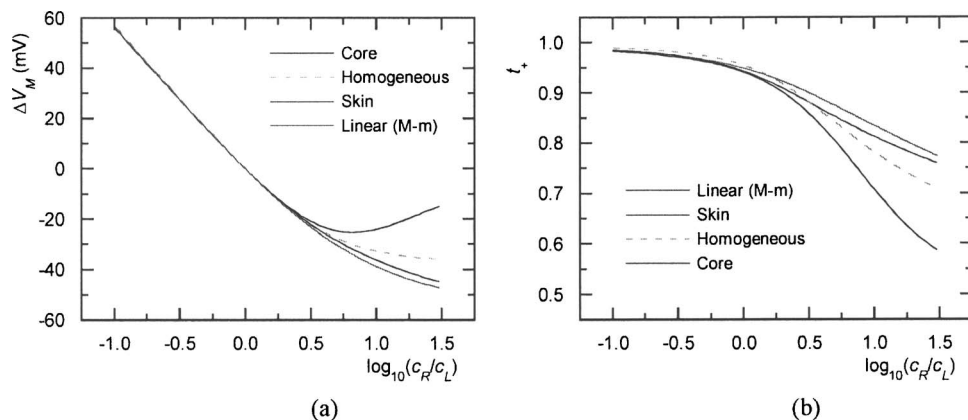
FIG. 4. Nanopore potential [Fig. 4(a)] and counterion transport number [Fig. 4(b)] vs the logarithm of the external concentration ratio for different fixed charge distributions (see Fig. 2) and $c_L = 0.1M$.

the different inhomogeneous distributions. This procedure gives $X_M = 0.891M$ [skin, Fig. 2(b)], $0.370M$ [wide clusters, Fig. 2(c)], $0.438M$ [narrow clusters, Fig. 2(d)], and $0.937M$ [linear, Fig. 2(e)]. In order to compare the linear [Fig. 2(e)] and hyperbolic [Fig. 2(f)] distributions, we have assumed $X_M = 0.937M$ and $X_m = 0.04M$ in Fig. 2(f), giving now $X_{avg} = 0.132M$. This allows a better comparison of the pore entrance effects, which are dominant for transport, as it will be shown later.

The I-V curves for the symmetrical [Fig. 3(a)] and asymmetrical [Fig. 3(b)] nanopore fixed charge distributions of Fig. 2 clearly show that a spatial redistribution of a constant amount of fixed charges leads to significantly different results. The currents in Fig. 3(a) follow the series skin > homogeneous > clusters and core distributions because the resistance at the nanopore entrance, which is determined by the local mobile ion concentrations, dictates the value of the current. However, this is not the only factor influencing the current, since the particular alternate arrangement of high and low resistance regions in Fig. 2 is also significant. Figure 3(b) shows that asymmetric fixed charge distributions lead to rectifying, diodelike behaviors (continuous curves). As in Fig. 3(a), the resistances at the nanopore entrances dictate the electric current. Therefore, higher currents are obtained when the ions enter the nanopore end with the higher charge [see the insets in Fig. 3(b)], which explains the rectifying effects. The calculated currents are higher for the linear distribution than for the hyperbolic distribution because of the higher average fixed charge distribution of the linear case. The dashed lines in Fig. 3(b) correspond to homogeneous charge

distributions with the same average concentrations as in the linear case ($X_{avg} = 0.5M$) and the hyperbolic case ($X_{avg} = 0.132M$).

Figure 4 shows the nanopore potential [Fig. 4(a)] and the counterion transport number [Fig. 4(b)] versus the logarithm of the external concentration ratio for different fixed charge distributions. This electric potential difference appears for $I = 0$ when the external electrolyte solutions are kept at different concentrations. The transport number is a measure of the nanopore selectivity to the counterion[35] and can be written in terms of the nanopore potential as

$$t_i = 0.5\left[1 - z_i \frac{F}{RT}\frac{\Delta V_M}{\ln(c_R/c_L)}\right]. \tag{16}$$

For negatively charged nanopores, $t_+ > 0.5 > t_-$, with t_+ close to unity in the limit of high fixed charge concentrations. In Fig. 4, $c_L = 0.1M$ while c_R is changed from 10^{-2} to $3M$. Two regimes are clearly seen in Figs. 4(a) and 4(b): at low electrolyte concentrations (with respect to the average fixed charge concentration), the Nernstian[35] linear behavior is obtained; at high concentrations, however, significant differences appear among the charge distributions, mainly because of the different interfacial Donnan potentials in each case [see Figs. 1(a) and 2]. The values of these potential differences lead to the selectivity scale skin > linear $M - m$ > homogeneous > core distributions. The core distribution shows a lower selectivity because of the relatively low fixed charge concentrations at the nanopore ends and the concomitant low Donnan potentials. On the contrary, the high charge
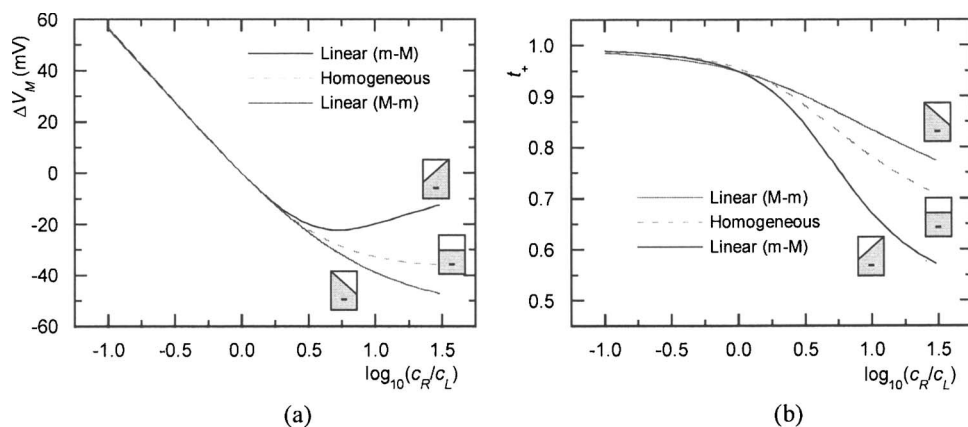

FIG. 5. Nanopore potential [Fig. 5(a)] and counterion transport number [Fig. 5(b)] vs the logarithm of the external concentration ratio ($c_L = 0.1M$) for the two different orientations of the linear fixed charge distribution shown in the insets.
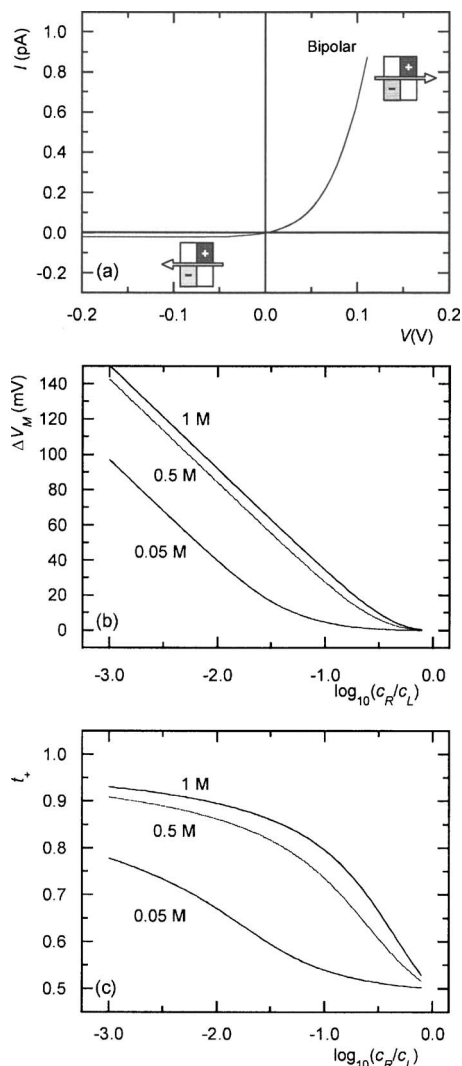
FIG. 6. *I-V* curve [Fig. 6(a); $c_L = c_R = 0.1M$], nanopore potential [Fig. 6(b); $c_L = 0.1M$], and cation transport number [Fig. 6(c)] for a bipolar fixed charge distribution formed by a negative region juxtaposed in series to a positive region. The diffusion coefficients of the ionic species are assumed to be $D_{K^+} = D_{Cl^-} \approx 2 \times 10^{-5}$ cm^2/s. All figures are obtained with X_N (negative region) $= X_P$ (positive region) for the fixed charge concentration and $d_N = d_P = 5$ μm for the thickness. In Fig. 6(a), $X_N = 1M$, while in Figs. 6(b) and 6(c) the curves are parametric in X_N.

FIG. 7. Experimental *I-V* curves for the symmetric double-conical [Fig. 7(a); unpublished results], asymmetric conical [Fig. 7(b); Ref. 11], and cylindrical [Fig. 7(c); Ref. 9] nanopores with thickness $d = 12$ μm. The curves of Fig. 7(a), which are parametric in $pH_L = pH_R$, are obtained with $c_L = c_R = 1M$ KCl. The curves of Fig. 7(b) are parametric in the KCl concentration. The curves of Fig. 7(c) are obtained with $c_L = c_R = 0.1M$ KCl, $pH_L = 8$, and $pH_R = 2$. The insets show the nanopore radii and schematic fixed charge distributions.

concentrations at the nanopore ends yield high selectivities for the skin and linear distributions, with the homogeneous nanopore showing intermediate results.

It is remarkable that asymmetry effects can also be noticed in the nanopore potential. Figure 5 shows that the nanopore selectivity depends on the orientation of the linear fixed charge distribution with respect to the concentration difference imposed in the external solutions. Again, this effect arises from the different Donnan potentials [see Fig. 1(b)] in each case. The lower selectivity is obtained for the $m-M$ case because increasing c_R decreases the value of the higher Donnan potential $\Delta\phi_R$ in Eq. (4b). On the contrary, increasing c_R does not change the higher Donnan potential $\Delta\phi_L$ in Eq. (4a) for the $M-m$ case. Therefore, not only the asymmetry of the nanopore but also the asymmetry of the external solutions dictates the observed selectivity. This is not the case for the symmetrical nanopore where the selectivity is dictated exclusively by the nanopore characteristics.
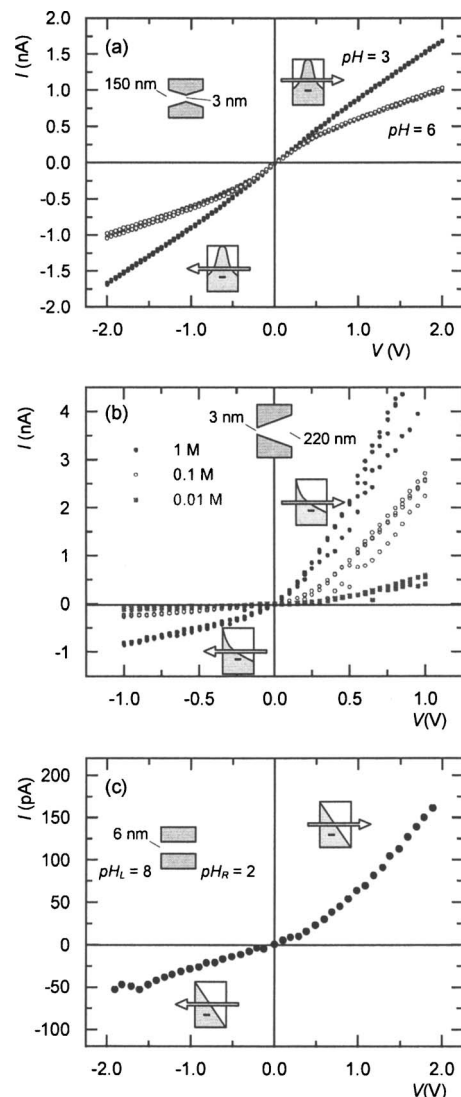
An extreme case of asymmetry is that of a bipolar nanopore [Fig. 6(a)] where negative and positive fixed charge distributions are arranged in series. Bipolar junctions are relevant in nanopores,[48–50] membrane separation processes,[30] and biological membranes.[26] Relatively simple analytic expressions for the *I-V* curve and the nanopore potential are available for the particular case of symmetric bipolar junctions.[30] Typical results are given in Figs. 6(a)–6(c). The forward and reverse bias regimes of Fig. 6(a) show high rectification, with a clear limiting current for $V < 0$, as experimentally confirmed.[51] The curves of Figs. 6(b) and 6(c) are parametric in the fixed charge concentrations of the negative and positive regions [see the insets in Fig. 6(a)]. The nanopore potential of Fig. 6(b) is now dictated by the interfacial Donnan potential at the bipolar junction.[31,52] The decrease of this potential at high electrolyte concentrations
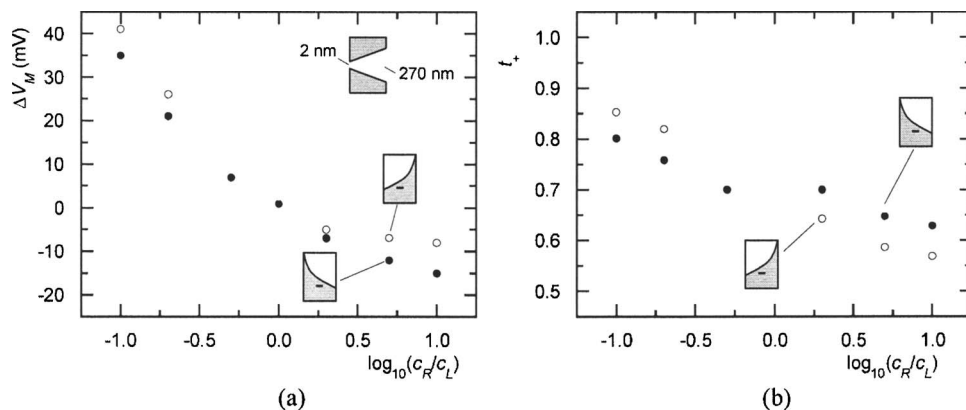
FIG. 8. Experimental nanopore potential [Fig. 8(a); unpublished results] and counterion transport number [Fig. 8(b); unpublished results] of a conical nanopore vs the logarithm of the external concentration ratio and $c_L = 0.1M$ KCl and $d = 12$ μm. Two different orientations of the asymmetric fixed charge distribution are shown in the insets.

yields to lower selectivities in this limit, as shown in Fig. 6(c). This decrease becomes less significant as the fixed charge concentrations at the bipolar junction becomes higher.

We compare now the above theoretical predictions with recent experimental data, emphasizing those qualitative aspects characteristic of each particular fixed charge distribution. Figure 7 shows the experimental I-V curves for the symmetric double-conical [Fig. 7(a)], asymmetric conical [Fig. 7(b)], and cylindrical [Fig. 7(c)] nanopore geometries. The double-conical nanopore should roughly correspond to the core distribution of Fig. 2(a). The curves of Fig. 7(a) (unpublished results) were obtained with the experimental setup described previously[11] for the case of a double-conical nanopore. These curves are parametric in the solution pH to emphasize the effect of the nanopore fixed charges: the weak-acid groups are protonated at low pH [and then $X(x) \approx 0$] and deprotonated at intermediate pH values. The I-V curves show no rectification, as expected for a symmetrical nanopore bathed by identical external solutions. However, the I-V curve deviates from the linear behavior at intermediate pH values because of the axial inhomogeneity of the fixed charge distribution, in agreement with the results corresponding to the core distribution of Fig. 3(a) (see also the experimental results of Ref. 53). The experimental data of Fig. 7(b) were reported in a recent study.[11] The curves are parametric in the electrolyte concentration and show the effect of the mobile charges in the nanopore solution. Rectification effects arise now because of the conical nanopore geometry resulting in an approximately hyperbolic fixed charge distribution [the linear distribution provides also the same qualitative trends; see the respective curves in Fig. 3(b)]. The experimental data of Fig. 7(c) were taken from Ref. 9 and clearly show that a pH difference ($pH_L = 8$ and $pH_R = 2$) externally imposed can force a symmetric (cylindrical) nanopore to behave as an asymmetrical one because of the resulting fixed charge inhomogeneity[9] [see again Fig. 3(b) for
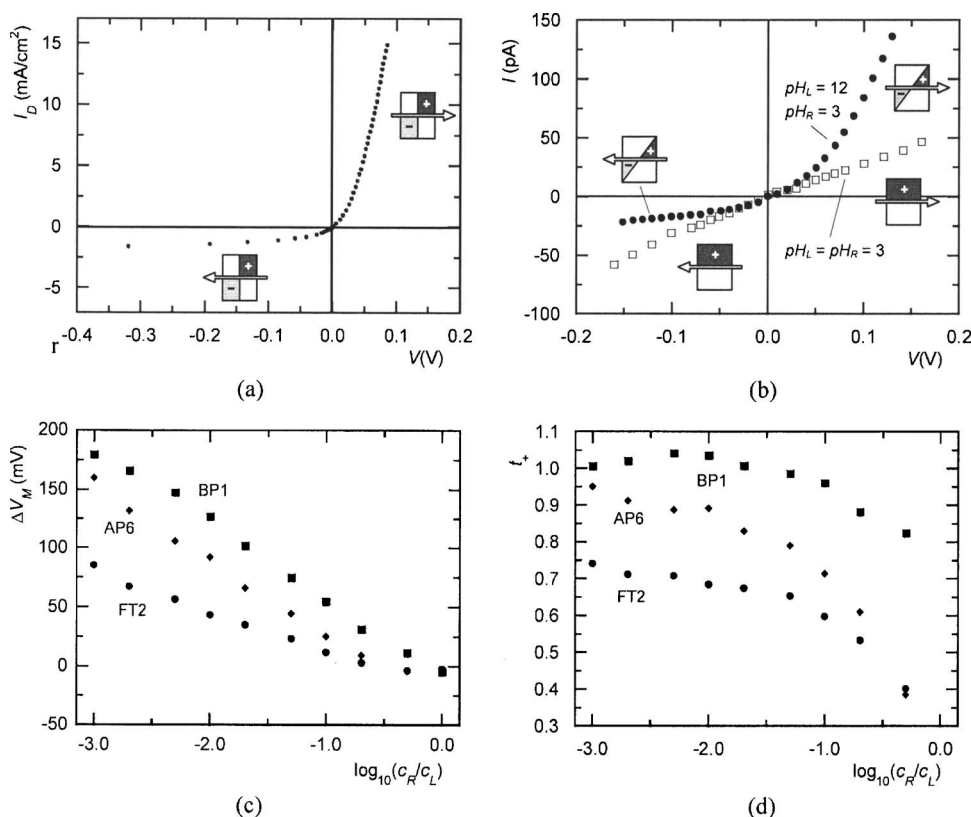

FIG. 9. Experimental I-V curves [Fig. 9(a), Ref. 51, and Fig. 9(b), Ref. 26], membrane potentials [Fig. 9(c); Ref. 52], and cation transport numbers [Fig. 9(d)] for different commercial membranes [Figs. 9(a), 9(c), and 9(d)] and the OmpF ion channel [Fig. 9(b)]. In Fig. 9(a), $c_L = c_R = 1M$ Na$_2$SO$_4$. In Fig. 9(b), $c_L = c_R = 0.1M$ KCl, with pH_L and pH_R indicated in the insets. In Figs. 9(c) and 9(d), $c_L = 1M$ KCl (see Refs. 26, 51, and 52 for details).

comparison]. Note that in this case the nanopore end at neutral pH is negatively charged while the other end facing the acidic solution remains neutral.

Figure 8 shows the experimental nanopore potential [Fig. 8(a)] and the counterion transport number [Fig. 8(b)] of a conical nanopore versus the logarithm of the external concentration ratio (unpublished results). Two different orientations of the asymmetric fixed charge distribution with respect to the external solutions are considered, as shown in the respective insets. As theoretically predicted in Fig. 5 for the case of the linear distribution, two regimes are clearly seen in Figs. 8(a) and 8(b). The Nernstian linear behavior results at low electrolyte concentrations while orientation-dependent selectivities are obtained at high concentrations. Note that the selectivities of Fig. 8(b) are lower than those in Fig. 5(b) because the nanopore is only weakly charged in our experiments.

Figure 9 shows other experimental *I-V* curves[26,51] [Figs. 9(a) and 9(b)], membrane potentials[52] [Fig. 9(c)], and cation transport numbers [Fig. 9(d)]. The results of Figs. 9(a), 9(c), and 9(d) were obtained with several commercial bipolar membranes while those of Fig. 9(b) correspond to the biological ion channel outer membrane porin F (OmpF, one of the general diffusion porins of *E. coli*; see Refs. 24 and 26). In the latter case, the ion channel charge distribution changes from symmetrical (monopolar) to asymmetrical (bipolar here) because of an externally imposed pH difference (see the insets). Clearly, the qualitative features of Figs. 9(a), 9(c), and 9(d) are well reproduced by the theoretical curves of Figs. 6(a)–6(c), respectively. Remarkably, the *I-V* curve of the ion channel [Fig. 9(b)] resembles that of a bipolar junction when pH$_L$=3 and pH$_R$=12 [see Fig. 6(a)] because of the protonated (positively charged) groups and deprotonated (negatively charged) groups placed at the respective ends of the nanopore in this case (see Ref. 26 for details). As expected, this externally induced bipolar nature is virtually lost when the bathing solutions are identical (pH$_L$=3=pH$_R$).

IV. CONCLUSIONS

We have estimated theoretically the effects that spatially inhomogeneous fixed charge distributions exert on the ionic transport and selectivity properties of nanopores immersed in electrolyte solutions. A complete survey of one-dimensional distributions (the skin, core, cluster, and asymmetric cases) exhibiting spatial variation over the macroscopic nanopore length has been analyzed on the basis of the Nernst-Planck equations. Current-voltage curves, membrane potentials, and transport numbers have been calculated in an attempt to ascertain whether an appropriate design of the spatial fixed charge inhomogeneity could lead to an enhancement of the transport and selectivity with respect to the homogeneous nanopore case. To this end, the results have systematically been compared with those obtained for the case of a homogeneous nanopore with the same average fixed charge concentration. Also, the model predictions have been contrasted with relevant experimental data. Since nanopores with fixed charges display properties that resemble those found in pro-

tein ion channels such as ionic selectivity and current rectification, the results may also be relevant for biological membranes.

[1] B. Hille, *Ionic channels of excitable membranes* (Sinauer, Sunderland, 2001).
[2] K.-Y. Chun and P. Stroeve, Langmuir **18**, 4653 (2002).
[3] J.-R. Ku and P. Stroeve, Langmuir **20**, 2030 (2004).
[4] K.-Y. Chun, S. Mafé, P. Ramírez, and P. Stroeve, Chem. Phys. Lett. **418**, 561 (2006).
[5] R. Fan, R. Karnik, M. Yue, D. Li, A. Majumdar, and P. Yang, Nano Lett. **5**, 1633 (2005).
[6] D. Fologea, J. Uplinger, B. Thomas, D. S. Mcnabb, and J. Li, Nano Lett. **5**, 1734 (2005).
[7] A. J. Storm, J. H. Chen, H. W. Zandbergen, and C. Dekker, Phys. Rev. E **71**, 051903 (2005).
[8] R. Karnik, K. Castelino, R. Fan, P. Yang, and A. Majumdar, Nano Lett. **5**, 1638 (2005).
[9] A. Fuliński, I. D. Kosińska, and Z. Siwy, Europhys. Lett. **67**, 683 (2004).
[10] J. Cervera, B. Schiedt, and P. Ramírez, Europhys. Lett. **71**, 35 (2005).
[11] J. Cervera, B. Schiedt, R. Neumann, S. Mafé, and P. Ramírez, J. Chem. Phys. **124**, 104706 (2006).
[12] Z. Siwy, I. D. Kosińska, A. Fuliński, and C. R. Martin, Phys. Rev. Lett. **94**, 048102 (2005).
[13] I. D. Kosinska, J. Chem. Phys. **124**, 244707 (2006).
[14] C. Selvey and H. Reiss, J. Membr. Sci. **23**, 11 (1985).
[15] S. A. Kuehl and R. D. Sanderson, J. Phys. Chem. **92**, 517 (1988).
[16] J. A. Manzanares, S. Mafé, and J. Pellicer, J. Phys. Chem. **95**, 5620 (1991).
[17] J. A. Manzanares, S. Mafé, and J. Pellicer, J. Chem. Soc., Faraday Trans. **88**, 2355 (1992).
[18] S. Koter, J. Membr. Sci. **108**, 177 (1995).
[19] J.-P. Hsu, K.-C. Ting, and Y.-H. Shieh, J. Phys. Chem. B **104**, 3492 (2000).
[20] R. Yamamoto, H. Matsumoto, and A. Tanioka, J. Phys. Chem. B **107**, 10615 (2003).
[21] M. Higa and T. Yamakawa, J. Phys. Chem. B **108**, 16703 (2004).
[22] E.-Y. Choi, H. Strathmann, J.-M. Park, and S.-H. Moon, J. Membr. Sci. **268**, 165 (2006).
[23] I. Kosztin and K. Schulten, Phys. Rev. Lett. **93**, 238102 (2004).
[24] A. Alcaraz, E. M. Nestorovich, M. Aguilella-Arzo, V. M. Aguilella, and S. M. Bezrukov, Biophys. J. **87**, 943 (2004).
[25] M. Aguilella-Arzo, J. Cervera, P. Ramírez, and S. Mafé, Phys. Rev. E **73**, 041914 (2006).
[26] A. Alcaraz, P. Ramírez, E. García-Giménez, M. L. López, A. Andrio, and V. M. Aguilella, J. Phys. Chem. B **110**, 21205 (2006).
[27] P. Y. Apel, Y. E. Korchev, Z. Siwy, R. Spohr, and M. Yoshida, Nucl. Instrum. Methods Phys. Res. B **184**, 337 (2001).
[28] Z. Siwy and A. Fuliński, Am. J. Phys. **72**, 567 (2004).
[29] K. Lebedev, S. Mafé, and P. Stroeve, J. Phys. Chem. B **109**, 14523 (2005).
[30] P. Ramírez, H. J. Rapp, S. Reíchle, H. Strathmann, and S. Mafé, J. Appl. Phys. **72**, 259 (1992).
[31] P. Ramírez and S. Mafé, Acta Polym. **48**, 234 (1997).
[32] S. Lee, Y. Zhang, H. S. White, C. C. Harrel, and C. R. Martin, Anal. Chem. **76**, 6108 (2004).
[33] B. Schiedt, K. Healy, A. P. Morrison, R. Neumann, and Z. Siwy, Nucl. Instrum. Methods Phys. Res. B **236**, 109 (2005).
[34] R. S. Eisenberg, J. Membr. Biol. **150**, 1 (1996).
[35] N. Lakshminarayanaiah, *Equations of Membrane Biophysics* (Academic, New York, 1984).
[36] R. Larter, Chem. Rev. (Washington, D.C.) **90**, 355 (1990).
[37] Z. Siwy, Y. Gu, H. A. Spohr, D. Baur, A. Wolf-Reber, R. Spohr, P. Apel, and Y. E. Korchev, Europhys. Lett. **60**, 349 (2002).
[38] Z. Siwy, P. Apel, D. Dobrev, R. Neumann, R. Spohr, C. Trautmann, and K. Voss, Nucl. Instrum. Methods Phys. Res. B **208**, 143 (2003).
[39] P. Ramírez, S. Mafé, V. M. Aguilella, and A. Alcaraz, Phys. Rev. E **68**,

011910 (2003).

[40] P. Ramírez, S. Mafé, A. Alcaraz, and J. Cervera, J. Phys. Chem. B **107**, 13178 (2003).

[41] S. Mafé, J. Pellicer, and V. M. Aguilella, J. Phys. Chem. **90**, 6045 (1986).

[42] A. D. MacGillivray, J. Chem. Phys. **48**, 2903 (1968).

[43] V. García-Morales, J. Cervera, and J. A. Manzanares, J. Electroanal. Chem. **599**, 203 (2007).

[44] W. H. Press, B. P. Flannery, S. A. Teukolsky, and W. T. Vetterling, *Numerical Recipes* (Cambridge University Press, Cambridge, 1989).

[45] J. Pellicer, S. Mafé, and V. M. Aguilella, Ber. Bunsenges. Phys. Chem. **90**, 867 (1986).

[46] P. Ramírez, A. Alcaraz, and S. Mafé, J. Membr. Sci. **135**, 135 (1997).

[47] J.-R. Ku, S.-M. Lai, N. Ileri, P. Ramírez, S. Mafé, and P. Stroeve, J. Phys. Chem. C **111**, 2965 (2007).

[48] H. Daiguji, Y. Oka, and K. Shirono, Nano Lett. **5**, 2274 (2005).

[49] R. Karnik, C. Duan, K. Castelino, H. Daiguji, and A. Majumdar, Nano Lett. **7**, 547 (2007).

[50] I. Vlassiouk and Z. S. Siwy, Nano Lett. **7**, 552 (2007).

[51] P. Ramírez, H.-J. Rapp, S. Mafé, and B. Bauer, J. Electroanal. Chem. **375**, 101 (1994).

[52] A. Alcaraz, P. Ramírez, S. Mafé, H. Holdik, and B. Bauer, Polymer **41**, 6627 (2000).

[53] C. Ho, R. Qiao, J. B. Heng, A. Chatterjee, R. J. Timp, N. R. Aluru, and G. Timp, Proc. Natl. Acad. Sci. U.S.A. **102**, 10445 (2005).